



Two-dimensional pseudo-phase-equilibrium approach on the cathode gas diffusion layer of proton exchange membrane fuel cell under varying degrees of humidification

Ken-Ming Yin*, Hsiao-Kuo Hsuen, Chih-Hsuan Hsu

Department of Chemical Engineering and Materials Science, Yuan Ze University, Chung-Li, Taoyuan 32003, Taiwan

HIGHLIGHTS

- ▶ A novel pseudo-phase equilibrium function is proposed in 2-D fuel cell model.
- ▶ Explicit water front tracking in the cathode gas diffuser is unnecessary.
- ▶ 2-D performance was validated by the 1-D model where analytical solution was available.
- ▶ Dynamic responses of water transport were analyzed.

ARTICLE INFO

Article history:

Received 31 July 2012

Received in revised form

26 January 2013

Accepted 30 January 2013

Available online 6 February 2013

Keywords:

Proton exchange membrane fuel cell

Pseudo-phase-equilibrium approach

Humidification

Water management

Liquid water front

ABSTRACT

We propose a novel 2D water management for cathodes of proton exchange membrane fuel cells (PEMFCs). A pseudo-phase-equilibrium function is incorporated to the model to relate the vapor fraction to the liquid water within the cathode gas diffusion layer, so that explicit tracking of the liquid water front between the single phase and two-phase domains becomes completely unnecessary. In the proposed model, liquid water transport in the porous medium is governed by the capillary pressure gradient, whereas the multi-component gas transports of oxygen, nitrogen, and water vapor are described using the Stefan–Maxwell equations. The effects of the gas diffusion layer thickness, porosity, temperature, pressure, and varying degrees of feed humidification are investigated. In addition to the steady-state performance, the dynamic response is computed for a detailed exploration of both the oxygen diffusion and the transient water imbibition and drainage. It concludes that the proposed method can be successfully applied to the two-phase fuel cell models in 2D geometry for both the steady-state and dynamic analyses.

© 2013 Elsevier B.V. All rights reserved.

1. Introduction

Proton exchange membrane fuel cells (PEMFCs) are considered possible power source that will replace the combustion engine in transportation vehicles [1]. PEMFC byproducts are water and heat, and there are no gas emissions. The solid polymer electrolyte used in the cell allows PEMFCs to fit into a constraint space, so that it is suitable for portable electronics, such as laptops or mobile phones. Technical hurdles, such as a limited resource of platinum catalysts and stringent conductivity and stability requirements of the solid electrolyte employed, must be overcome to make PEMFCs commercially viable [2]. Structural optimization of the membrane electrode assembly (MEA) is important for optimal use of the cell

component materials [3]. In practice, improved cell performance is possible if the MEA design conforms to better water management [4]. Although moist environments are indispensable to the facilitation of electrochemical reactions in the respective anode and cathode catalyst layers, excessive water generation at high current densities floods the cathode diffusion layer. Once the cathode diffusion layer is severely flooded, oxygen transport limitation prohibits a further increase of current.

Because an in-situ observation on the gaseous species and liquid water distribution are difficult and expensive [5,6], mathematical models were proposed to characterize the important operating parameters affecting the PEMFC performance. Because a cell operates on open circuit voltage (OCV) until it reaches high cell overpotential, a completely dry diffusion layer to the co-existence of one-phase and two-phase domains is expected. The amount of liquid water and the location of the liquid water front

* Corresponding author. Tel.: +886 3 4638800x2556; fax: +886 3 4559373.

E-mail address: cekenyin@saturn.yzu.edu.tw (K.-M. Yin).

depend on the specified cell temperature, pressure, and inlet humidification [7]. A versatile mathematical model should be able to identify the onset current density of liquid water and location of the liquid water front within the gas diffusion layer. Nguyen and co-workers [8–10] adopted unsaturated flow theory (UFT), formulating the conservation equations for the respective gaseous species and liquid water. They tracked the local vapor pressure using a switch function, toggling between water evaporation and condensation. Thus, explicit determination of the liquid water front was bypassed, and elaborating on the formulation of the interior boundary condition was avoided. This approach was extended to the treatment of the micro-porous layer and the catalyst layer [11,12], and it was also used for transient analysis [13–17]. Although the switch function devised by Nguyen and co-workers [8–11] treats the liquid water front easily, the associated evaporation and condensation rate constants are not well defined. In general, large values for the evaporation and condensation rate constants are presumed to approximate the instantaneous phase equilibrium conditions. Another approach, tailored by Wang and co-workers, was called the multi-phase mixture model (M^2). This approach was used to transport the gaseous and liquid water [18–21]. It solves a single set of transport equations for a mixed fluid with averaged physical properties; whereas the individual velocities of gaseous and liquid phases are extracted after the solution is completed. An M^2 approach is limited to a sink-free or source-free domain, and confined to a Darcy type transport formulation [22]. Both approaches used the capillary head as the driving force for the liquid permeation in the two-phase region, but various capillary pressure formulations appeared in the literature. Vynnycky determined the liquid water front explicitly in a 1D model [23], in which the mass conservation equations were imposed at the interface. Chupin et al. [24] proposed a pseudo-2D model (1D through the MEA and 1D along the channel), considering liquid water front tracking. An analytical formulation on the liquid water front was obtained by Hsuen and Yin [7], who assigned the same values of the binary gas-pair diffusivities of the water vapor to nitrogen and oxygen. The deviation of the cell performance was found to be non-significant if the same diffusivities were assumed. Although a direct calculation of the water front is feasible, the numerical complexities multiply as multi-dimensional problems are encountered, which is one reason the UFT method coupled with evaporation/condensation switching and the M^2 method were widely adopted in the literature.

A conceptually different method named the pseudo-phase-equilibrium approach was demonstrated in a steady-state 1D model for the PEMFC cathode compartment [25], in which an approximate phase equilibrium function was introduced in the gas diffusion layer. The 1D result was validated by the analytical solution, where the liquid water front was determined directly. Liquid water is always assumed to be present in the gas diffusion layer governed by the phase equilibrium function in the pseudo-phase-equilibrium approach, and tracking the liquid water front is avoided for the entire operation. This approach is extended to a 2D model across the MEA, as shown in Fig. 1. This approach is further extended to the dynamic response, as shown in the paper. A transient study of the vehicle operation during acceleration and deceleration is critical [26]. To focus on the mathematical framework, water transfer across the membrane is described by a constant electro-osmotic drag coefficient; that is, the membrane hydration/dehydration effect is not considered.

2. Mathematical formulations

Schematic of the modeling domain on the cathode compartment of MEA is depicted in Fig. 1. The gas diffusion layer is

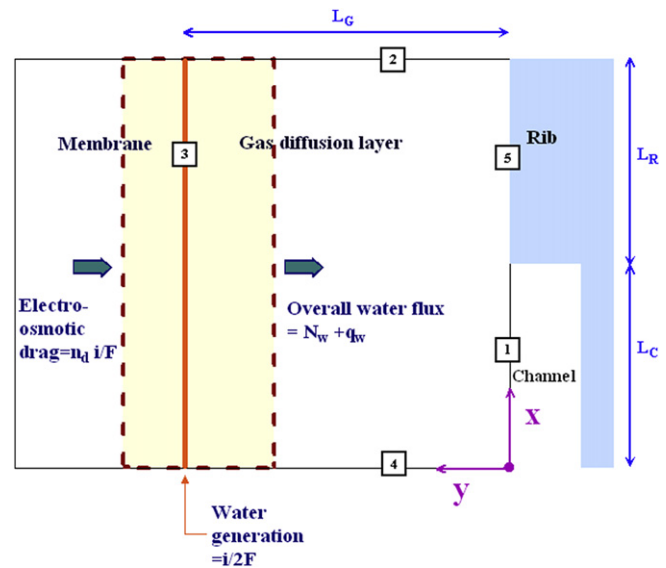


Fig. 1. Schematic diagram of the cathode compartment of PEMFC. N_w : vapor flux, q_w : liquid water flux, n_d : electro-osmotic drag coefficient, i : local current density.

supported on the bi-polar plate grooved with flow channel for oxygen supply. As shown, water conservation over the dash-line enclosed area indicates that total water flux ($N_w + q_w$) through the gas diffusion layer is attributed by the water generation rate within the catalyst layer ($i/2F$), plus that crossed over the membrane by electro-osmotic drag ($n_d i/F$). Total water flux is attributed by the liquid water flux (q_w) and vapor flux (N_w). Since pseudo-phase-equilibrium is satisfied over the entire gas diffusion layer, it is not necessary to identify the current density where the liquid water emerges. Hence the explicit liquid water front tracking is avoided. The following derived governing equations and associated boundary conditions are solved by the finite element solver Comsol Multiphysics [27].

Major assumptions in the model are listed:

- (i) The gas diffusion layer is isothermal and isobaric.
- (ii) Capillary pressure established in the gas diffusion layer is the only driving force for liquid water transport.
- (iii) Nitrogen flux is zero in the gas diffusion layer since it is an inert species.
- (iv) Catalyst layer is regarded as a thin layer without thickness.
- (v) The electro-osmotic drag coefficient of water in the membrane is constant.
- (vi) Ideal gas law is applied to the gaseous phase in the gas diffusion layer.
- (vii) Ohmic loss in the carbon phase is negligible.
- (viii) The deformation of gas diffusion layer due to compression and intrusion and its effect on gas and water transport are not considered.
- (ix) Stefan–Maxwell equations describe multi-component gas transport in the gas diffusion layer. In addition, effective binary gas diffusivities are evaluated using the Bruggeman expression [28].

In Section 2.1, mass conservation equations are derived for the feed with unsaturated vapor. The equations for the feed with saturated vapor in Section 2.2 are reduced from Section 2.1. Table 1 lists kinetic parameters used in the model unless otherwise specified.

Table 1
Parameters used in the base case unless otherwise specified.

Half channel width, L_C (cm)	0.05
Half rib width, L_R (cm)	0.05
Gas diffusion layer thickness, L_G (cm)	0.03
Porosity of gas diffusion layer (wet proofed pores), ε_0	0.5 [28]
Cell temperature, T (K)	353
Cathode pressure, P_c (atm)	5
Gas-pair diffusivity, $D_{O_2-N_2}$ ($\text{cm}^2 \text{s}^{-1}$)	$D_{O_2-N_2} = \frac{0.273}{P} \left(\frac{T}{T_{\text{ref}}} \right)^{1.823}$ [33]
Gas-pair diffusivity, D_{N_2-w} ($\text{cm}^2 \text{s}^{-1}$)	$D_{N_2-w} = \frac{0.387}{P} \left(\frac{T}{T_{\text{ref}}} \right)^{1.823}$ [33]
Gas-pair diffusivity, D_{O_2-w} ($\text{cm}^2 \text{s}^{-1}$)	$D_{O_2-w} = \frac{0.37}{P} \left(\frac{T}{T_{\text{ref}}} \right)^{1.823}$ [33]
Liquid viscosity, μ_w ($\text{g cm}^{-1} \text{s}^{-1}$)	$3.565 \times 10^{-3} - \frac{(T-353)}{20} (4.71 \times 10^{-3} - 3.565 \times 10^{-3})$ [34]
Liquid density, ρ_w (g cm^{-3})	$0.972 - \frac{(T-353)}{20} (0.983 - 0.972)$ [34]
Liquid absolute permeability, $K_{\text{I,abs}}$ (cm^2)	3×10^{-10} [34]
δ (adjustable parameter in phase equilibrium function, Eq. (6))	0.03
Electro-osmotic drag coefficient (n_d)	1.59 [35]
Cathode transfer coefficient, (α_c)	1 [36–38]
<i>Parameters in capillary pressure head expression</i>	
A	3.7 [8]
B	21 [8]
C	0.494 [8]
D (cm)	0.0173 [8]
$i_{0,\text{ref}} \gamma$ (A cm^{-2})	1×10^{-6} [25,39,40]

2.1. Feed with unsaturated water vapor

The equations of continuity in the gas diffusion layer for oxygen and water are as follows:

$$\frac{\partial [\varepsilon_0(1-s)c_t x_{O_2}]}{\partial t} + \nabla \cdot N_{O_2} = 0 \quad (1)$$

$$\frac{\partial [\varepsilon_0(1-s)c_t x_w]}{\partial t} + \nabla \cdot N_w + \frac{\varepsilon_0 \rho_w}{m_w} \frac{\partial s}{\partial t} + \nabla \cdot q_w = 0 \quad (2)$$

where ε_0 is porosity in the GDL, x_{O_2} and x_w are the respective oxygen and vapor mole fractions, c_t is the total gas concentration, s is the liquid water saturation, ρ_w is liquid density, m_w is water

molecular weight, N_{O_2} and N_w are the respective oxygen and water vapor fluxes, and q_w is the liquid water flux.

The flux expression for gaseous species is described by the Stefan–Maxwell equation as shown below [28]:

$$\nabla x_i = \sum_{j=1}^n \frac{1}{c_t D_{i-j}^{\text{eff}}} (x_i N_j - x_j N_i) \quad (3)$$

x_i is the mole fraction of i , N_i is the flux of i , D_{i-j}^{eff} is the effective binary gas diffusivity for pair i and j . The effective gas diffusivity is adopted from Bruggeman expression [28]:

$$D_{i-j}^{\text{eff}} = D_{i-j} [\varepsilon_0(1-s)]^{1.5} \quad (4)$$

The pseudo-phase-equilibrium between vapor and liquid is always satisfied within the diffusion layer, approximated by Ref. [25]

$$x_w = x_w^{\text{sat}} [1 - \exp(-bs)] \quad (5)$$

where

$$b = -\frac{\ln \delta}{\delta} \quad (6)$$

where x_w^{sat} is the saturated vapor fraction, defined as $x_w^{\text{sat}} = P_w^{\text{sat}}/P_c$. P_c is the gas pressure in the cathode gas diffusion layer. Saturated vapor pressure P_w^{sat} is expressed as a function of absolute temperature [29]

$$\ln(P_w^{\text{sat}}) = 70.434643 - \frac{7362.6981}{T} + 0.006952085T - 9 \ln T \quad (7)$$

δ is a parameter that quantifies the departure of the present approximation from the exact one [25]. Eqs. (5) and (6) were formulated by considering that $x_w = 0$ for $s = 0$ and $x_w = x_w^{\text{sat}}(1-\delta)$ for $s = \delta$. For exact phase equilibrium, δ is zero and b approaches infinity. Thus, a smaller value of δ indicates that Eq. (5) is closer to the exact one.

For the transport of oxygen and water vapor, Stefan–Maxwell equations are further simplified with the condition $N_{N_2} = 0$:

$$c_t \nabla x_{O_2} = \frac{1}{D_{O_2-w}^{\text{eff}}} (x_{O_2} N_w - x_w N_{O_2}) - \frac{1}{D_{O_2-N_2}^{\text{eff}}} (x_{N_2} N_{O_2}) \quad (8)$$

$$c_t \nabla x_w = \frac{1}{D_{O_2-w}^{\text{eff}}} (x_w N_{O_2} - x_{O_2} N_w) - \frac{1}{D_{w-N_2}^{\text{eff}}} (x_{N_2} N_w) \quad (9)$$

The mole fraction of nitrogen is governed by the constraint $x_{N_2} = 1 - x_{O_2} - x_w$. Eqs. (5), (8) and (9) can be rearranged to give Eqs. (10) and (11) for the flux expressions of oxygen and water vapor:

$$N_{O_2} = \frac{\left(\frac{x_{O_2}}{D_{O_2-w}} + \frac{1 - x_{O_2} - x_w^{\text{sat}} [1 - \exp(-bs)]}{D_{w-N_2}} \right) c_t [\varepsilon_0(1-s)]^{1.5} \nabla x_{O_2} + \frac{x_{O_2} x_w^{\text{sat}} b \exp(-bs) c_t [\varepsilon_0(1-s)]^{1.5} \nabla s}{D_{O_2-w}^{\text{eff}}} - \left(\frac{x_{O_2}}{D_{O_2-w}} + \frac{1 - x_{O_2} - x_w^{\text{sat}} [1 - \exp(-bs)]}{D_{w-N_2}} \right) \left(\frac{x_w^{\text{sat}} [1 - \exp(-bs)]}{D_{O_2-w}} + \frac{1 - x_{O_2} - x_w^{\text{sat}} [1 - \exp(-bs)]}{D_{O_2-N_2}} \right)}{(D_{O_2-w})^2} \quad (10)$$

$$N_w = \frac{\frac{x_w^{\text{sat}} [1 - \exp(-bs)]}{D_{O_2-w}} c_t [\varepsilon_0(1-s)]^{1.5} \nabla x_{O_2} + \left(\frac{x_w^{\text{sat}} [1 - \exp(-bs)]}{D_{O_2-w}} + \frac{1 - x_{O_2} - x_w^{\text{sat}} [1 - \exp(-bs)]}{D_{O_2-N_2}} \right) \frac{x_w^{\text{sat}} b \exp(-bs) c_t [\varepsilon_0(1-s)]^{1.5} \nabla s}{D_{O_2-w}^{\text{eff}}} - \left(\frac{x_{O_2}}{D_{O_2-w}} + \frac{1 - x_{O_2} - x_w^{\text{sat}} [1 - \exp(-bs)]}{D_{w-N_2}} \right) \left(\frac{x_w^{\text{sat}} [1 - \exp(-bs)]}{D_{O_2-w}} + \frac{1 - x_{O_2} - x_w^{\text{sat}} [1 - \exp(-bs)]}{D_{O_2-N_2}} \right)}{(D_{O_2-w})^2} \quad (11)$$

Liquid water flux in the gas diffusion layer is driven by the capillary head [8]:

$$q_w = \frac{-K(s)\rho_w^2 g}{\mu_w m_w} \left(-\frac{\partial \psi}{\partial s} \right) \nabla s \quad (12)$$

$K(s)$ is relative liquid permeability in the gas diffusion layer, g is the gravitational acceleration, ψ is the capillary head, μ_w is liquid water viscosity.

ψ and $K(s)$ are expressed as [8]:

$$\psi = \left[\left(e^{-A(s-C)} - e^{A(s-C)} \right) + B \right] D \quad (13)$$

$$K(s) = K_{l,abs}(s + 0.01) \quad (14)$$

A, B, C, D are parameters based on the materials property of the gas diffusion layer [11]; values in Ref. [8] are adopted here. $K_{l,abs}$ is the absolute liquid permeability. Eq. (12) can then be simplified to Eq. (15)

$$q_w = \frac{K_{l,abs}\rho_w^2 g A D (s + 0.01) [e^{-A(s-C)} + e^{A(s-C)}]}{\mu_w m_w} \nabla s \quad (15)$$

Eqs. (1) and (2) coupled with Eqs. (10), (11) and (15) can be used to solve the dynamic responses of x_{O_2} and s . Stationary solutions are obtained by removing the time dependent terms in Eqs. (1) and (2).

Boundary conditions

At boundary 1:

$$x_{O_2} = x_{O_2,b} = 0.21(1 - x_w^{\text{sat}} \text{RH}), \quad (16)$$

$$s = s_0 = -\frac{\ln(1 - \text{RH})}{b} \quad (17)$$

$x_{O_2,b}$ is the oxygen fraction in the feed, while 0.21 is oxygen fraction on a dry basis. RH is the relative humidity in the feed.

Boundaries 2 and 4 are the symmetric lines:

$$\frac{\partial x_{O_2}}{\partial x} = 0, \quad (18)$$

$$\frac{\partial s}{\partial x} = 0 \quad (19)$$

Boundary 3 is the active surface for the catalyst layer:

$$N_{O_2} = -\frac{i}{4F}, \quad (20)$$

$$N_w + q_w = \left(\frac{1}{2} + n_d \right) \frac{i}{F} \quad (21)$$

Eq. (20) states that the flux of oxygen is consumed by the electrochemical reaction, while Eq. (21) indicates the total water flux is attributed by the water generated by reaction plus that dragged from the membrane.

There is no species across boundary 5.

$$\frac{\partial x_{O_2}}{\partial y} = 0, \quad (22)$$

$$\frac{\partial s}{\partial y} = 0 \quad (23)$$

n_d is the electro-osmotic drag coefficient, and local current density $i(=|i|)$ can be expressed by the Tafel kinetics:

$$i = i_0 \gamma (1 - s) \frac{c_t x_{O_2}}{c_{O_2,ref}} \exp \left(\frac{-\alpha_c F \eta_c}{RT} \right) \quad (24)$$

i_0 is the exchange current density corresponding to the reference oxygen concentration $c_{O_2,ref}$ and the cell temperature T , γ is the roughness factor defined as the active area per MEA apparent area, α_c is the apparent cathodic transfer coefficient. The cathode electrode overpotential η_c is defined as the potential difference between the cathode potential V_c and the cathode open circuit potential [28]:

$$\eta_c = V_c - 1.23 + 0.9 \times 10^{-3} (T - 298) - \frac{RT}{4F} \ln(P_{O_2}) \quad (25)$$

The dependency of i_0 on temperature was formulated by Parthasarathy et al. [30]:

$$i_0 = i_{0,ref} \exp \left[\frac{-73269}{R} \left(\frac{1}{T} - \frac{1}{T_{ref}} \right) \right] \quad (26)$$

$i_{0,ref}$ is the reference exchange current density corresponding to the reference oxygen concentration $c_{O_2,ref}$ and the reference temperature T_{ref} . The cell current density is obtained by averaging local current density i over the active surface:

$$I = \frac{\int_0^L i \, dx}{L} \quad (27)$$

L is the length of repeating unit on the active surface, as depicted in the x -direction shown in Fig. 1.

2.2. Cathode feed with saturated vapor

The conservation equations for oxygen and water are the same as Eqs. (1) and (2). Since saturated vapor is supplied, $x_w = x_w^{\text{sat}}$ and $\nabla x_w = 0$ can be inserted into Eqs. (8) and (9), which can be reduced:

$$\nabla x_{O_2} = \frac{1}{c_t D_{O_2-w}^{\text{eff}}} \left(x_{O_2} N_w - x_w^{\text{sat}} N_{O_2} \right) - \frac{1}{c_t D_{O_2-N_2}^{\text{eff}}} x_{N_2} N_{O_2} \quad (28)$$

$$N_w = \left(\frac{\frac{x_w^{\text{sat}}}{D_{O_2-w}}}{\frac{x_{O_2}}{D_{O_2-w}} + \frac{x_{N_2}}{D_{w-N_2}}} \right) N_{O_2} \quad (29)$$

Eq. (29) is substituted into Eq. (28) and combined with $x_{N_2} = 1 - x_{O_2} - x_w^{\text{sat}}$

$$N_{O_2} = \frac{\left(\frac{x_{O_2}}{D_{O_2-w}} + \frac{1 - x_{O_2} - x_w^{\text{sat}}}{D_{w-N_2}} \right) c_t [\varepsilon_0 (1 - s)]^{1.5} \nabla x_{O_2}}{\frac{x_{O_2} x_w^{\text{sat}}}{(D_{O_2-w})^2} - \left(\frac{x_{O_2}}{D_{O_2-w}} + \frac{1 - x_{O_2} - x_w^{\text{sat}}}{D_{w-N_2}} \right) \left(\frac{x_w^{\text{sat}}}{D_{O_2-w}} + \frac{1 - x_{O_2} - x_w^{\text{sat}}}{D_{O_2-N_2}} \right)} \quad (30)$$

Eq. (30) is inserted into Eq. (29)

$$N_w = \frac{\frac{x_w^{\text{sat}}}{D_{O_2-w}} c_t [\varepsilon_0 (1-s)]^{1.5} \nabla x_{O_2}}{\frac{x_{O_2} x_w^{\text{sat}}}{(D_{O_2-w})^2} - \left(\frac{x_{O_2}}{D_{O_2-w}} + \frac{1-x_{O_2}-x_w^{\text{sat}}}{D_{w-N_2}} \right) \left(\frac{x_w^{\text{sat}}}{D_{O_2-w}} + \frac{1-x_{O_2}-x_w^{\text{sat}}}{D_{O_2-N_2}} \right)} \quad (31)$$

Eq. (15) is adopted for the liquid water flux.

Boundary conditions

At boundary 1:

$$x_{O_2} = x_{O_2,b} \quad (32)$$

$$s = 0 \quad (33)$$

Boundary conditions on surfaces 2 and 4 are the same as Eqs. (18) and (19).

Boundary conditions on surface 3 are the same as Eqs. (20) and (21).

Boundary conditions on surface 5 are the same as Eqs. (22) and (23).

3. Results and discussion

3.1. Effects of parameter δ

Fig. 2 depicts the simulated polarization curves using different values of δ for both the 1D and 2D models at a cell-operating temperature of 80 °C, a cathode pressure of 5 atm, and inlet relative humidity set at 0.5. As shown in past work [25], using a smaller parameter δ indicated a better approximation to the exact phase

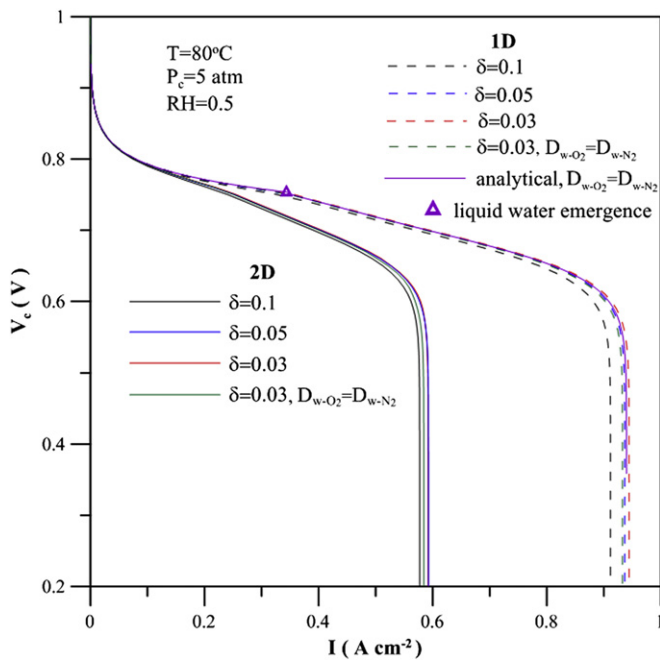


Fig. 2. Influence of parameter δ on the prediction of cell performance for 1-D and 2-D simulations. Analytical solution is only available for 1-D model with assumption $D_{w-O_2} = D_{w-N_2}$. Symbol Δ indicates the location of liquid water emergence (0.3441, 0.7536) determined from the analytical solution. $T = 80$ °C, $RH = 0.5$, $P_c = 5$ atm.

equilibrium. Fig. 2 shows the prediction of an enhanced performance, as δ is decreased from 0.1 to 0.03 for both the 1D and 2D models. Hsuen and Yin [25] recognized that the binary diffusivities of D_{w-O_2} and D_{w-N_2} differ slightly. With the approximation $D_{w-O_2} \approx D_{w-N_2}$, they were able to obtain analytical solutions for the 1D model. The 1D analytical solutions for the given operating conditions are included for comparison. The liquid water emerging in the gas diffusion layer, with the same diffusivity approximation, was analytically determined at (0.3441, 0.7536) and marked with a triangle symbol. The numerical solution to the 1D model using the pseudo-phase-equilibrium approach with $\delta = 0.03$ can be compared to the one with the same diffusivity assumption ($D_{w-O_2} \approx D_{w-N_2}$). Only minor discrepancies are shown to have been incurred by the different values of diffusivity and δ . The 2D model predicted a performance that was inferior to the 1D case caused by the blocking effect of the rib. It showed non-significant differences in the polarization curves for δ less than 0.05. For comparison, the result of the $D_{w-O_2} \approx D_{w-N_2}$ approximation is also included in the 2D case. Similar to the 1D case, only minor differences were observed if the same diffusivity assumption was used. The 1D and 2D models had identical predictions near the open circuit potential, suggesting only minor effects of the rib in such a regime.

Fig. 3 shows the cross-profiles of the water saturation and oxygen fraction in the gas diffusion layer for the 1D model at a specified potential of 0.6 V. A better approximation was obtained by reducing the value of δ . The exact liquid front at the 0.6 V potential with the assumption $D_{w-O_2} \approx D_{w-N_2}$ was analytically calculated at the dimensionless distance of 0.379 from the gas diffusion layer/channel interface. Oxygen diffused through the diffusion layer and depleted near the active surface. A smaller δ predicted less water saturation and a higher oxygen fraction in the diffusion layer, consistent with the prediction of better performance in Fig. 2. Fig. 4 depicts the concentration profiles on the cross-section at the symmetry line $x = 0$ for the 2D case. Similar trends and almost identical numerical values for the water saturation and oxygen fraction were predicted as those in the 1D case, suggesting that the influence of the rib on species distribution was non-significant over the area away from the recessed region.

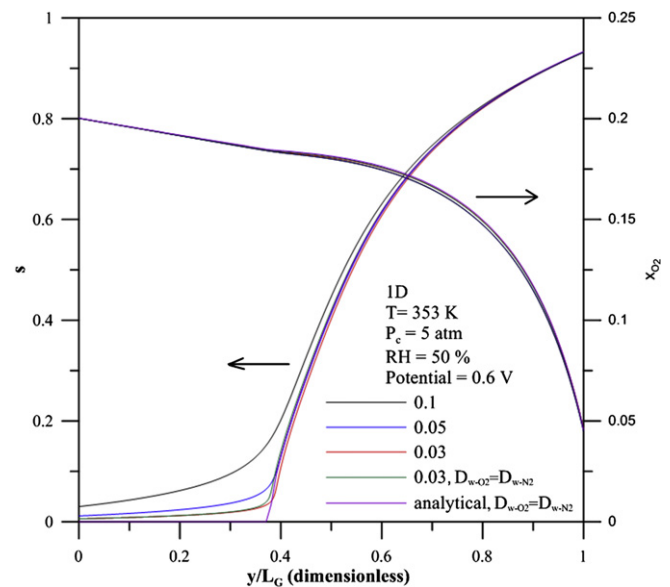


Fig. 3. Effect of parameter δ on water saturation and oxygen fraction profiles across the gas diffusion layer in 1-D model. Key is the same as in Fig. 2.

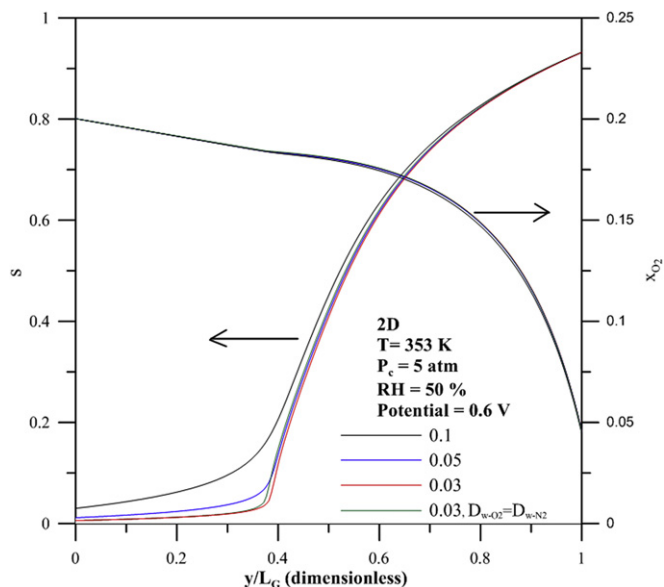


Fig. 4. Effect of parameter δ on water saturation and oxygen fraction profiles at $x = 0 \text{ cm}$ in 2-D model. Key is the same as in Fig. 2.

3.2. Effect of gas diffusion layer thickness

Fig. 5 shows the prediction of better performance when a thinner gas diffusion layer was used. As shown, the effect of layer thickness was negligible near the open circuit potential where electrode activation overpotential dominates. The limiting current densities for the gas diffusion layers at 100, 200, 300, and 400 μm were 1.5156, 0.8331, 0.5922, and 0.4754 A cm^{-2} , respectively. This suggested that a shorter diffusion passage favors oxygen transport. The numerical ratio of two limiting current densities was less than the inverse ratio of their corresponding diffusion layer thicknesses. This implied that a thicker gas diffusion layer caused better

diffusion of oxygen in the in-plane direction into the recessed region over the rib. This effect became prominent at an increased polarization. The detailed local current density distribution along the catalyst layer depicted in Fig. 6 validated the cell current density in Fig. 5. In the figure, the non-significant effect of the diffusion layer thickness was observed in the activation-controlled regime at 0.8 V. As the cathode potential was reduced to 0.6 V, a higher local current density was predicted facing the channel if a thinner diffusion layer is used; whereas an opposite trend was observed in the region over the rib. It revealed that the through-plane diffusion dominated the overall reaction rate, which was favored by a thinner gas diffusion layer. In contrast, a thinner gas diffusion layer rendered a smaller cross-sectional area for the in-plane oxygen diffusion into the region between the catalyst surface and the shoulder. Thus, the utilization of the catalyst layer on the area facing the rib was much lower than that in the area facing the channel. The distributions of the oxygen fraction and liquid saturation at 0.6 V (plotted in Fig. 7), verified the current distribution, as shown in Fig. 6. For the comparison between 100 μm and 400 μm , a much higher oxygen gradient was observed near the catalyst layer above the channel for the thinner diffusion layer, while more oxygen was diffused into the region over the shoulder for the thicker diffusion layer. Water permeation within the porous medium is a sluggish process, and relatively high saturation was observed near the active surface and within the recessed region for both thicknesses at 0.6 V. Water accumulation within the diffusion medium prohibited efficient oxygen diffusion, and resulted in the subsequent mass transfer limitation. Water management of a thinner diffusion layer was improved because of a shorter through-plane transport length. The onsets of water emergence on the active surface in the 1D model with the assumption $D_{W-O_2} \approx D_{W-N_2}$ were determined analytically to be (1.0324, 0.7202), (0.5162, 0.7412), (0.3441, 0.7536), and (0.2581, 0.7623), corresponding to thicknesses of 100, 200, 300, and 400 μm , respectively. As indicated, water appearance occurred earlier for a thicker gas diffusion layer, caused by slower vapor diffusion and easier condensation allowing for a longer diffusion passage.

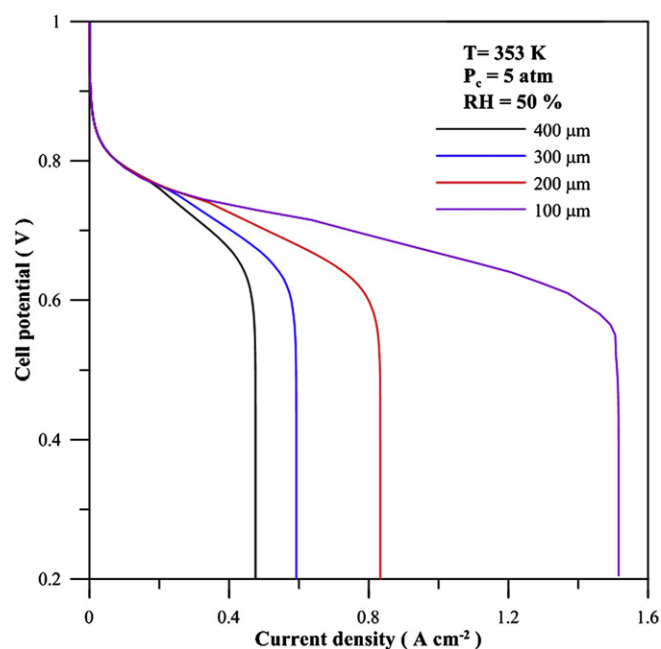


Fig. 5. Effect of gas diffusion layer thickness on the cell performance. $T = 80^\circ \text{C}$, $RH = 0.5$, $P_c = 5 \text{ atm}$, $\delta = 0.03$.

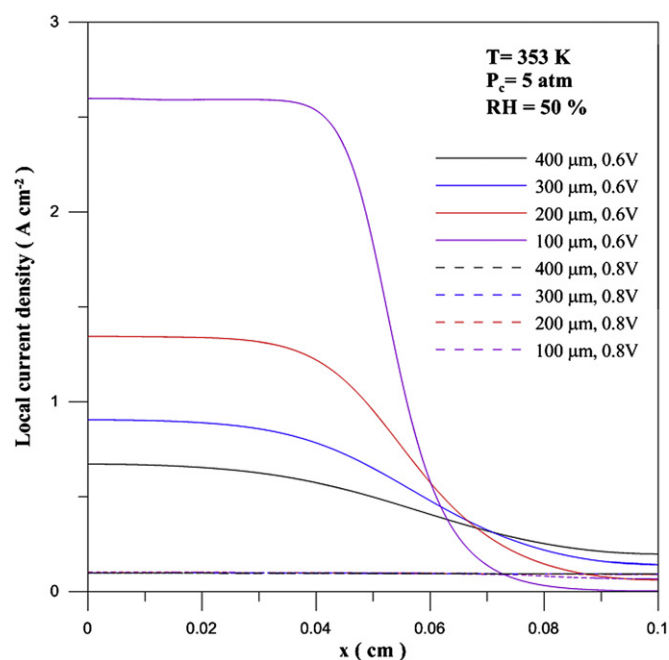


Fig. 6. Local current density distribution along the catalyst surface at $V_c = 0.6 \text{ V}$. $T = 80^\circ \text{C}$, $RH = 0.5$, $P_c = 5 \text{ atm}$, $\delta = 0.03$.

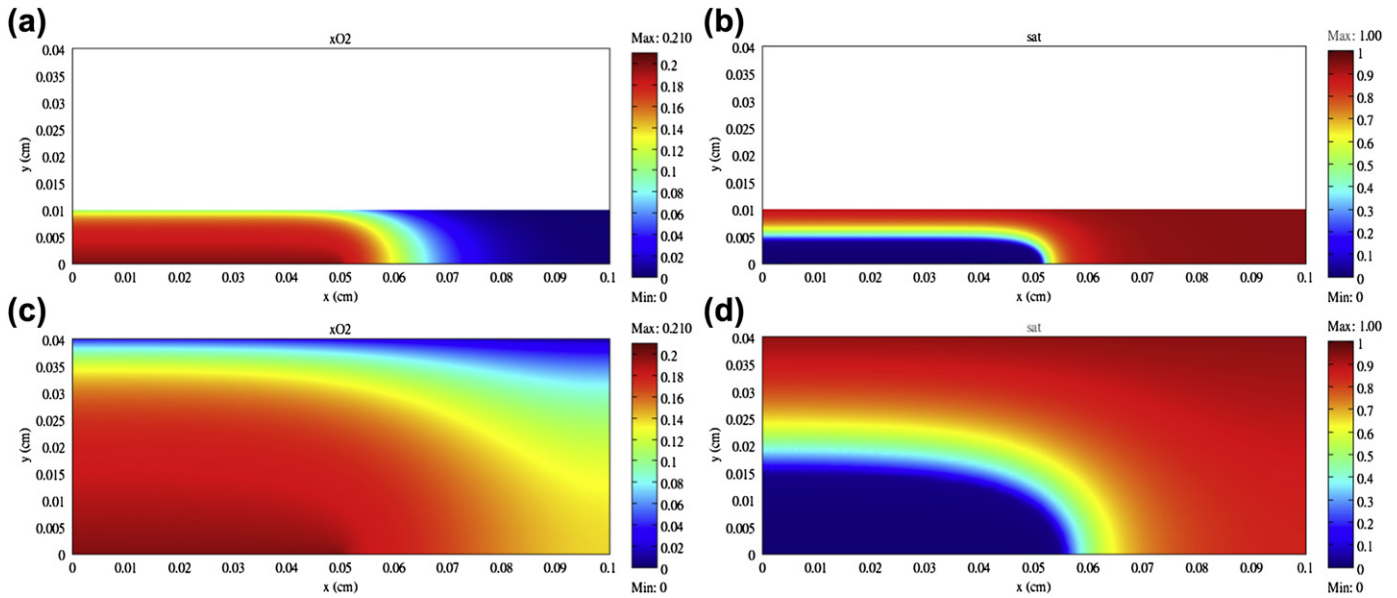


Fig. 7. Water saturation and oxygen fraction distributions within the gas diffusion layer for 100 and 400 μm at $V_c = 0.6$ V. (a) Oxygen, 100 μm , (b) liquid saturation, 100 μm , (c) oxygen, 400 μm , (d) liquid saturation, 400 μm .

3.3. Effect of varied degrees of humidification

Fig. 8 displays the performance at varied degrees of inlet humidification. For the unsaturated feed ($RH < 1$), the pseudo-phase-equilibrium approach equations detailed in Section 2.1 were used. The condensed equations given in Section 2.2 were used for the cathode feed with saturated vapor ($RH = 1$). An overall better performance was predicted as the inlet humidity was reduced, which was caused by less liquid accumulation and better oxygen diffusion within the gas diffusion layer. The membrane dehydration was not considered here, and its effects were not predicted. To

investigate the asymptotic behavior near $RH = 1$, the polarization predicted by the pseudo-phase-equilibrium approach at $RH = 0.99$ was also included, and showed a non-significant difference compared to the fully humidified feed. For complete picture of the water saturation and its effects on oxygen diffusion, the distributions at 0.6 V for $RH = 0$ and 1 are shown in Fig. 9. At $RH = 1$, excessive flooding was observed over the shoulder, and the water front was approaching the channel. In addition, oxygen depletion near the active surface, arising from the blockage of gas voids in the porous medium, was evident. For $RH = 0$, a higher oxygen fraction and less liquid flooding appeared in the gas diffusion layer. Because membrane dehydration was not considered in the study, the model result best described cell performance at high anode humidification and high current densities. As evidenced by the Wang et al. experiment [31], the cell performed better if lower cathode humidification was applied at a fully humidified anode feed.

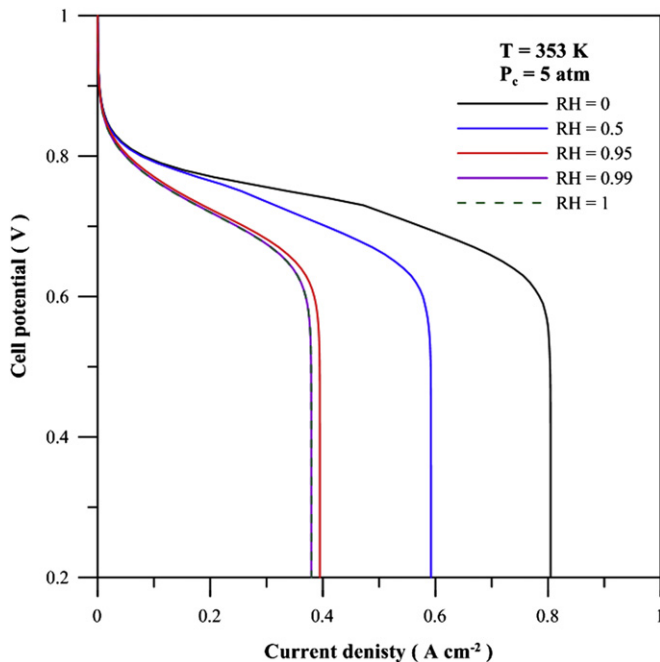


Fig. 8. Cell performance at various degrees of inlet humidification. $T = 80$ $^{\circ}\text{C}$, $P_c = 5$ atm, $\delta = 0.03$, gas diffusion layer thickness 300 μm .

3.4. Effect of cell temperature

The pseudo-phase-equilibrium approach is applicable to the non-isothermal condition, as long as an appropriate energy conservation equation is introduced. Eq. (5) is still required, and the parameters of gas diffusivity, electro-osmotic drag coefficient, and exchange current density should be expressed as a function of temperature. Here, the focus was on the isothermal condition. Fig. 10 predicted better cell performance if a higher cell temperature was specified. An increased temperature promotes the electrochemical kinetics of the catalyst, but it reduces the open circuit potential of the electrode. Gas diffusivity was increased, and mass transport limitation was extended to the region of the higher current densities. Because the vapor pressure was elevated, more vapors could be accommodated in the void space in the gas diffusion layer, and less liquid water was expected. Oxygen diffusion was more efficient because of the shrinkage of the two-phase domain. In an experiment by Yan et al. [32], the cell performance was improved as the cell temperature was raised when the cell temperature was lower than the humidification temperature, and the opposite was true if the cell temperature was higher than the humidification temperature. This theoretical study confirmed that

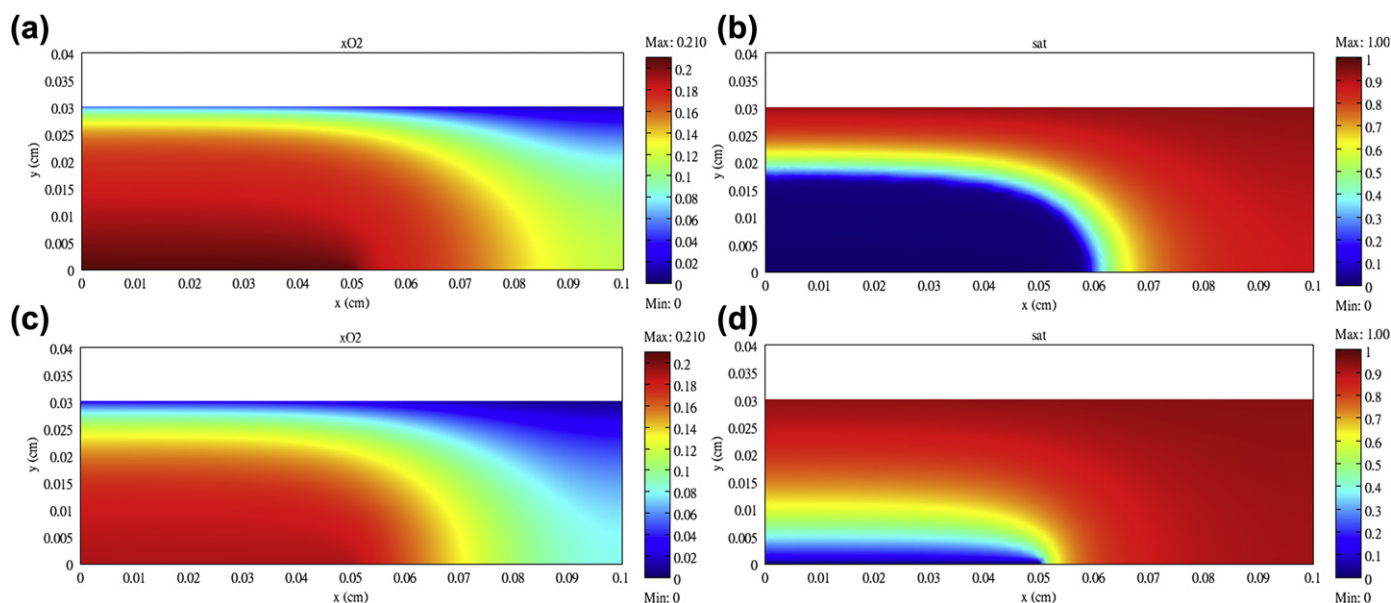


Fig. 9. Water saturation and oxygen fraction distributions within the gas diffusion layer for RH = 0 and 1 at $V_c = 0.6$ V. (a) Oxygen, RH = 0, (b) liquid saturation, RH = 0, (c) oxygen, RH = 1, (d) liquid saturation, RH = 1.

experiment; that is, for a cell temperature lower than the humidifier temperature, increasing the cell temperature enhances the electrode kinetics and mass transfer rate, if the membrane is maintained at a fully hydrated state.

3.5. Effect of cathode gas pressure

Fig. 11 illustrates the effect of pressure at the specified temperature of 80 °C and an inlet humidity of 0.5. Although the oxygen fraction was higher at the higher imposed cathode pressure, the gas diffusivity was reduced. At low polarization, an electrode with lower pressure performed better than that with higher pressure

because of the increased reactant concentration. As the current density was continuously increased, water flooded and the electrode became influenced by mass transfer. Because gas diffusivity is inversely proportional to the applied pressure, a reverse trend was observed at a higher polarization in contrast to that near the open circuit potential.

3.6. Effect of electrode porosity

The void fraction of the gas diffusion layer could be altered because of various pretreatments in the MEA fabrication. For example, carbon paper or cloth could be incorporated with

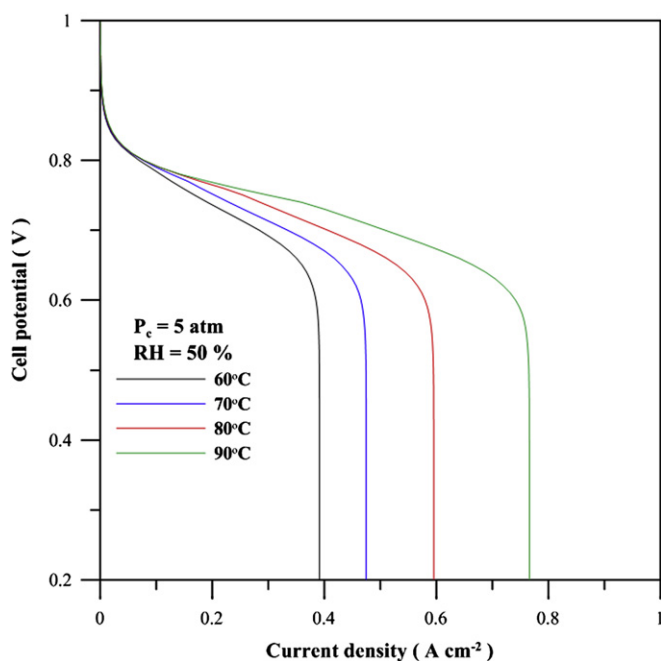


Fig. 10. Effect of temperature on cell performance. $P_c = 5$ atm, $RH = 0.5$.

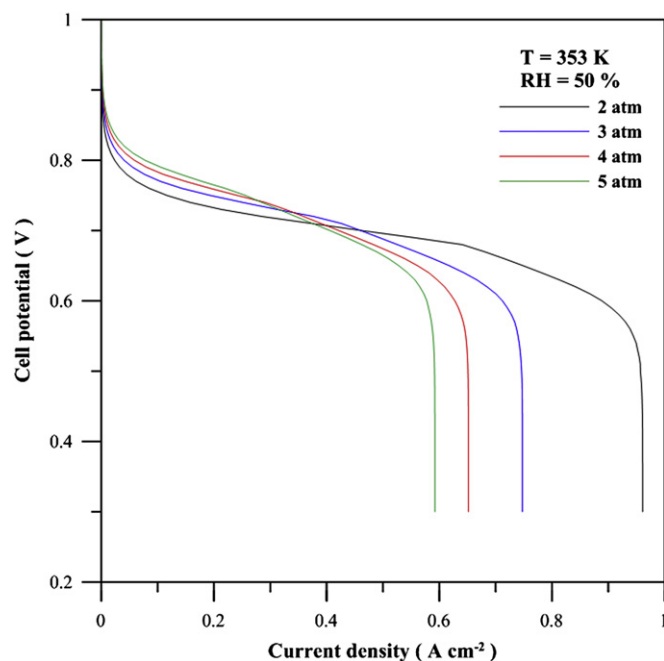


Fig. 11. Effect of pressure on cell performance. $T = 80$ °C, $RH = 0.5$.

a hydrophobic material such as poly(tetrafluoroethylene) (PTFE) for a better water drainage property. Thus, the porosity of the gas diffusion layer was changed by the material introduced. Fig. 12 depicts the effect of electrode porosity on cell performance. A non-significant effect was observed at low polarization where surface activation overpotential dominated. Larger porosity enhanced gas diffusion and delayed the emergence of liquid water. Consequently, the limiting current density was extended to a larger value.

3.7. Transient analysis

Cyclic voltammograms between 1.0 and 0.2 V, with different sweeping rates, are depicted in Fig. 13. Three cycles for each ramping rate were recorded. The results show that the periodic steady-state was reached during the second cycle, because the second and third cycles nearly overlapped. Because uniform concentrations of dried gases were used as the initial conditions in the calculation, the first cycle always exhibited larger current densities than the subsequent ones (especially in the forward scan). The dynamic response exhibited a maximum current density during the forward scan where the enhanced electrochemical kinetics was offset by the gradually accumulated water. Comparing the scan rates of 5 and 15 mV s^{-1} , higher peak current densities were observed for the case with a higher ramping rate, because of the shorter time period experienced for the production of water. As the periodic steady-state was reached, a slower sweep rate induced higher current densities near the open circuit potential in both the forward and backward scans. In the low polarization regime, where less water was generated and dragged from the membrane, a slower sweep rate gave water a longer period to drain in the gas diffusion layer. In the high polarization regime (cathode potential is less than 0.4 V), low sweep rates approximated a steady-state operation, and the limiting current density was approached.

Fig. 14 displays the detailed water saturation and oxygen fraction profiles on the symmetry line $x = 0$ cm at the cathode potential 0.6 V. For the specified voltage, higher water saturation

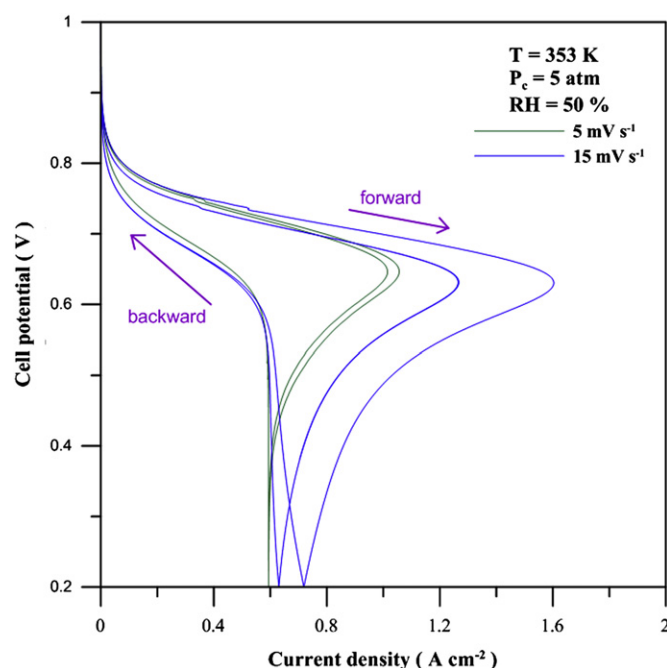


Fig. 13. Cyclic voltammograms at scan rates 5 and 15 mV s^{-1} for three consecutive cycles. $T = 80^\circ\text{C}$, $\text{RH} = 0.5$, $P_c = 5$ atm.

corresponded to a slower ramping rate in the forward scan. Because liquid transport is a relatively sluggish process, a low ramping rate resulted in severe flooding. The oxygen fraction profile was set in accordance with the liquid water distribution, and oxygen transfer was more efficient if the gas diffusion layer was less flooded. In the backward scan, only minor deviations on water saturation and oxygen fraction were detected among scan rates. This implied that the stationary behavior is approached after sufficiently long duration.

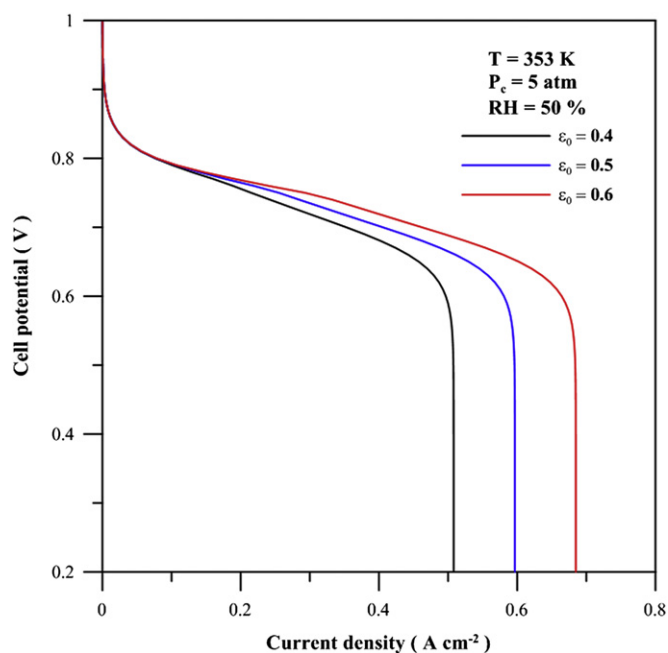


Fig. 12. Effect of porosity in cathode gas diffusion layer on the cell performance. $T = 80^\circ\text{C}$, $\text{RH} = 0.5$, $P_c = 5$ atm.

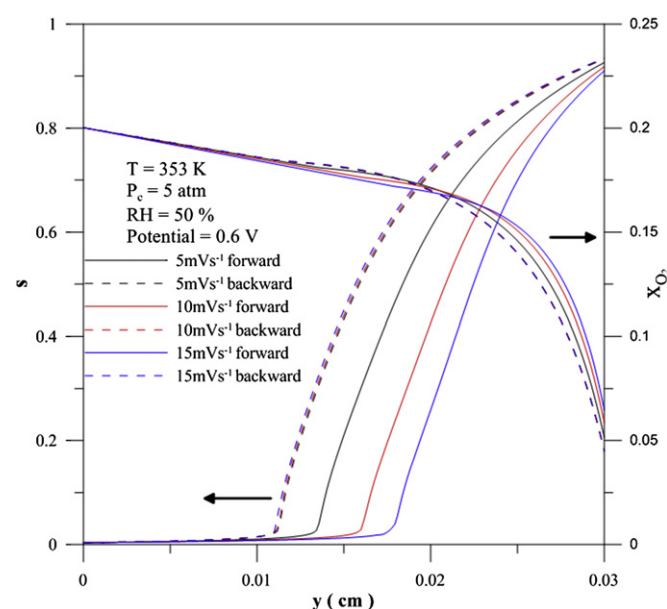


Fig. 14. Water saturation and oxygen fraction profiles at $x = 0$ cm and 0.6 V for varied scan rates. $T = 80^\circ\text{C}$, $\text{RH} = 0.5$, $P_c = 5$ atm. Solid line is for the forward scan and dashed line is for the backward scan.

4. Conclusion

A pseudo-phase-equilibrium approach was used for a 2D PEMFC simulation. The model accounted for multi-component gas and liquid water transport within the gas diffusion layer at varying degrees of humidification. This approach employed a phase-equilibrium function with a single adjustable parameter, avoiding the explicit tracking of the liquid water front. The 2D prediction showed a coherent trend with the accompanying 1D model. The 1D model with the same diffusivity assumption was included because this was the only case where the analytical solution is available.

The thinner gas diffusion layer performed better than the thicker one at the mass transfer influenced regime. Current was distributed uniformly along the active surface near the open circuit potential, irrespective of the diffusion layer thickness. A highly non-uniform current distribution was predicted in the near diffusion limited regime. As water flooded severely, thinner diffusion layers drained the water better in the region near the channel, despite the more difficult oxygen diffusion into the region over the shoulder.

Cell performance declined due to more moisture having been contained in the cathode feed because of the extensive water saturation and reduced oxygen fraction near the active surface. The pseudo-phase-equilibrium approach successfully predicted the asymptotic behavior of the fully humidified feed where the set of condensed equations in Section 2.2 should have been used.

Increased cell temperature enhanced overall cell performance. The effect of pressure differed depending on the operating conditions. Near the open circuit potential, high pressure raised the reactant concentration and enhanced the surface reaction rates. For the near mass transfer influenced regime, high pressure reduced gas diffusivity and resulted in a low limiting current density.

The dynamic response amplified the effects of the sluggish water transport process on cell performance. The peak current density in the forward scan indicated a counterbalance between the electrochemical kinetics enhanced by the increased overvoltage and the oxygen diffusion inhibited by the accumulated water. A higher peak current density resulted from higher sweep rates because of the shorter time required for water accumulation. Near the open circuit potential, in both the forward and backward scans, a slower sweep rate induced better performance than that with the higher rate. In such a regime where less water was produced, a longer duration improved water drainage. The pseudo-phase-equilibrium approach has been shown to be efficient and viable for multi-dimensional simulation on fuel cells, especially for the study of water management.

Acknowledgments

We are grateful for the financial supports by the Ministry of Education, the Office of Research and Development in Yuan Ze University through the available funds, and National Science Council of ROC (NSC 101-2221-E-155-046).

List of symbols

A	parameter in the capillary pressure head expression, Eq. (13)
b	parameter in the phase equilibrium equation, Eq. (5)
B	parameter in the capillary pressure head expression, Eq. (13)
$c_{O_2,ref}$	reference oxygen concentration, mol cm ⁻³
c_t	total gas concentration, mol cm ⁻³
C	parameter in the capillary pressure head expression, Eq. (13)
D	parameter in the capillary pressure head expression, Eq. (13), cm

D_{i-j}	binary diffusion coefficient for species i and j , cm ² s ⁻¹
D_{i-j}^{eff}	effective binary diffusion coefficient for species i and j , cm ² s ⁻¹
F	Faraday's constant, 96,487 C per equivalent
g	gravitational acceleration, 980 cm s ⁻²
i	local current density, A cm ⁻²
i_o	exchange current density with respect to T and $c_{O_2,ref}$, A cm ⁻²
$i_{o,ref}$	exchange current density with respect to T_{ref} and $c_{O_2,ref}$, A cm ⁻²
I	cathode current density, A cm ⁻²
K	liquid permeability in the gas diffusion layer, cm ²
$K_{l,abs}$	absolute liquid permeability in the gas diffusion layer, cm ²
L	integration length, cm
L_C	half channel width, cm
L_G	gas diffusion layer thickness, cm
L_R	half rib width, cm
m_w	water molecular weight, g mol ⁻¹
N_i	mole flux of species i , mol cm ⁻² s ⁻¹
P_c	cathode pressure, atm
p_w^{sat}	vapor pressure, atm
q_w	liquid water flux, mol cm ⁻² s ⁻¹
R	universal gas constant, 8.314 J mol ⁻¹ K ⁻¹
s	liquid saturation
T	cell temperature, K
T_{ref}	reference temperature, K
V_c	cathode potential, V
x_i	mole fraction of species i
$x_{O_2,b}$	mole fraction of oxygen in the channel
x_w^{sat}	mole fraction of saturated vapor

Greek letters

α_c	cathodic transfer coefficient
γ	roughness factor, cm ⁻¹
δ	parameter in the phase equilibrium function, Eq. (6)
ε_0	porosity of the gas diffusion layer
ψ	capillary head, cm
η_c	cathode overpotential, V
μ_w	viscosity of liquid water, g cm ⁻¹ s ⁻¹
ρ_w	density of liquid water, g cm ⁻³

References

- [1] S. Srinivasan, Fuel Cells: From Fundamentals to Applications, Springer, 2006.
- [2] F. Barbir, PEM Fuel Cells: Theory and Practice, Elsevier, 2005.
- [3] P. Costamagna, S. Srinivasan, J. Power Sources 102 (2001) 242–252.
- [4] P. Costamagna, S. Srinivasan, J. Power Sources 102 (2001) 253–269.
- [5] S. Tsushima, S. Hirai, Prog. Energy Combust. Sci. 37 (2011) 204–220.
- [6] A. Bazylak, Int. J. Hydrogen Energy 34 (2009) 3845–3857.
- [7] H.-K. Hsuen, K.-M. Yin, J. Power Sources 196 (2011) 218–227.
- [8] D. Natarajan, T.V. Nguyen, J. Electrochem. Soc. 148 (12) (2001) A1324–A1335.
- [9] W. He, J.S. Yi, T.V. Nguyen, AIChE J. 46 (2000) 2053–2064.
- [10] D. Natarajan, T.V. Nguyen, J. Power Sources 115 (2003) 66–80.
- [11] X. Wang, T.V. Nguyen, Electrochem. Soc. 155 (11) (2008) B1085–B1092.
- [12] M. Srinivasarao, D. Bhattacharyya, R. Rengaswamy, S. Narasimhan, J. Power Sources 195 (2010) 6782–6794.
- [13] H. Wu, P. Berg, X. Li, J. Electrochem. Soc. 157 (1) (2010) B1–B10.
- [14] C. Ziegler, H.M. Yu, J.O. Schumacher, J. Electrochem. Soc. 152 (8) (2005) A1555–A1567.
- [15] C. Ziegler, T. Heilmann, D. Gerteisen, J. Electrochem. Soc. 155 (4) (2008) B349–B355.
- [16] M. Zaglio, A. Wokaun, J. Mantzaras, F.N. Buchi, Fuel Cells 11 (2011) 526–536.
- [17] J. Hou, Int. J. Hydrogen Energy 36(1011) 7199–7206.
- [18] C.Y. Wang, P. Cheng, Int. J. Heat Mass. Transfer 39 (1996) 3607–3618.
- [19] Z.H. Wang, C.Y. Wang, K.S. Chen, J. Power Sources 94 (2001) 40–50.
- [20] Y. Wang, C.-Y. Wang, Electrochim. Acta 50 (2005) 1307–1315.
- [21] Y. Wang, K.S. Chen, J. Electrochem. Soc. 157 (12) (2010) B1878–B1886.
- [22] V. Gurau, T.A. Zawodzinski, J.A. Mann, ASME J. Fuel Cell. Sci. Technol. 5 (2008) 021009-1–021009-12.

- [23] M. Vynnycky, Appl. Math. Comput. 189 (2007) 1560–1575.
- [24] S. Chupin, T. Colinart, S. Didierjean, Y. Dube, K. Agbossou, G. Maranzana, O. Lottin, J. Power Sources 195 (2010) 5213–5227.
- [25] H.-K. Hsuen, K.-M. Yin, Int. J. Hydrogen Energy 36 (2011) 5487–5499.
- [26] K.H. Loo, K.H. Wong, S.C. Tan, Y.M. Lai, C.K. Tse, Int. J. Hydrogen Energy 35 (2010) 11861–11877.
- [27] COMSOL™ 3.5a, User's Guide, COMSOL AB, 2008.
- [28] D.M. Bernardi, M.W. Verbrugge, AIChE J. 37 (1991) 1151–1163.
- [29] J. Wishart, Z. Dong, M. Secanell, J. Power Sources 161 (2006) 1041–1055.
- [30] A. Parthasarathy, S. Srinivasan, J. Appleby, J. Electrochem. Soc. 139 (9) (1992) 2530–2537.
- [31] X.-D. Wang, Y.-Y. Duan, W.-M. Yan, F.-B. Weng, J. Power Sources 176 (2008) 247–258.
- [32] W.-M. Yan, X.-D. Wang, S.-S. Mei, X.-F. Peng, Y.-F. Guo, A. Su, J. Power Sources 185 (2008) 1040–1048.
- [33] R.B. Bird, W.E. Stewart, E.N. Lightfoot, Transport Phenomena, Wiley, New York, 1960.
- [34] H.-K. Hsuen, J. Power Sources 137 (2004) 183–195.
- [35] H.-K. Hsuen, K.-M. Yin, Electrochim. Acta 62 (2012) 447–460.
- [36] C. Marr, X. Li, J. Power Sources 77 (1999) 17–27.
- [37] J. Xie, F. Xu, D.L. Wood III, K.L. More, T.A. Zawodzinski, W.H. Smith, Electrochim. Acta 55 (2010) 7404–7412.
- [38] Y. Wang, C.-Y. Wang, J. Power Sources 147 (2005) 148–161.
- [39] N. Wagner, J. Appl. Electrochem. 32 (2002) 859–863.
- [40] C. Song, Y. Tang, J.L. Zhang, J. Zhang, H. Wang, J. Shen, S. McDermid, J. Li, P. Kozak, Electrochim. Acta 52 (2007) 2552–2561.